Journal of *Marine Science and Engineering*

MDPI

Article

A Super-Twisting Sliding-Mode Control Strategy for a Heaving Point Absorber Wave Energy Converter

Zhongfeng Li [1,2], Lixian Wang [1], Lidong Wang [1,*], Xiaoping Liu [3,*], Zhongyi Wang [1] and Lei Liu [2]

[1] School of Electronic and Information Engineering, University of Science and Technology Liaoning, Anshan 114051, China; afeng0601@163.com (Z.L.); wanglx_0515@163.com (L.W.); wangzhongyi0213@163.com (Z.W.)
[2] School of Electrical Engineering, Yingkou Institute of Technology, Yingkou 115100, China; liulei@yku.edu.cn
[3] College of Information Sciences and Engineering, Henan University of Technology, Zhengzhou 450001, China
* Correspondence: wangld5600@ustl.edu.cn (L.W.); liuxiaoping@haut.edu.cn (X.L.)

Abstract

This paper proposes a super-twisting sliding-mode control (STSMC) strategy to enhance the efficiency and stability of a heaving point absorber wave energy converter (PAWEC) system equipped with a permanent magnet synchronous generator (PMSG). In particular, the STSMC is designed to address both generator-side and grid-side control challenges by ensuring precise regulation under varying wave conditions. A dynamical model of the PAWEC is developed to describe system responses, while the power take-off (PTO) mechanism is tailored to maintain consistent generator speed and efficient energy conversion. Lyapunov stability theory is employed to verify the stability of the proposed controller. Simulation studies and tests on a small-scale experimental setup with a 500 W PAWEC model under regular and irregular waves demonstrate that STSMC improves generator speed regulation and power output by more than 30% compared to field-oriented control (FOC), nonlinear adaptive backstepping (NAB), and first-order sliding-mode control (FOSMC). The proposed approach also manages grid-side total harmonic distortion (THD) effectively, keeping it below 5%. These results indicate that STSMC can substantially improve the dynamic performance and energy efficiency of wave energy systems.

Keywords: point absorber wave energy converter; nonlinear dynamic modeling; power take-off control; permanent magnet synchronous generator; super-twisting sliding-mode control

check for updates

Academic Editor: Barbara Zanuttigh

Received: 29 April 2025
Revised: 16 June 2025
Accepted: 22 June 2025
Published: 23 June 2025

Citation: Li, Z.; Wang, L.; Wang, L.; Liu, X.; Wang, Z.; Liu, L. A Super-Twisting Sliding-Mode Control Strategy for a Heaving Point Absorber Wave Energy Converter. *J. Mar. Sci. Eng.* **2025**, *13*, 1214. https://doi.org/10.3390/jmse13071214

Copyright: © 2025 by the authors. Licensee MDPI, Basel, Switzerland. This article is an open access article distributed under the terms and conditions of the Creative Commons Attribution (CC BY) license (https://creativecommons.org/licenses/by/4.0/).

1. Introduction

Ocean wave energy has emerged as a promising renewable resource, driving advancements in wave energy converter (WEC) technologies [1,2]. Point absorber WECs (PAWECs) stand out due to their space-efficient structure and operational flexibility across diverse marine environments [3,4]. A persistent problem in practical PAWEC systems is the difficulty of maintaining stable and efficient power output when exposed to irregular, rapidly changing, and nonlinear wave forces. These fluctuations can cause significant variations in the generator's performance, reduce energy capture efficiency, and lead to unstable grid-side power quality, especially for systems using permanent magnet synchronous generators (PMSGs) and grid-connected power take-off (PTO) units. These systems utilize vertically oscillating buoys coupled with PTO mechanisms to convert wave motion into electrical energy [5,6]. Recent studies have proposed various control strategies to address these challenges and improve the performance of PAWECs under stochastic sea conditions [7,8].

The wave-to-wire modeling paradigm presents unique control challenges across energy conversion stages. Ref. [9] identifies three critical limitations in conventional approaches: simplified hydrodynamic coupling, linearized PTO dynamics, and decoupled electrical modeling. High-fidelity models such as those proposed by Penalba and Ringwood increase computational complexity for real-time control; however, this challenge can be mitigated using state-space modeling of convolution terms under harmonic input assumptions, as shown by Kristiansen et al. [10]. Spectral-domain approaches [11] enable efficient frequency-domain analysis yet struggle with transient wave conditions. These modeling compromises directly impact control performance—simplified models degrade maximum power point tracking (MPPT) accuracy by 15–20% under irregular waves [12], while detailed models introduce latency incompatible with sliding-mode techniques.

Field-oriented control (FOC) has been widely adopted in WECs for its straightforward implementation and computational efficiency [13]. Its decoupled flux–torque control architecture enables precise generator regulation under steady-state conditions [14]. While effective in controlled environments [15], FOC's linear framework struggles with the nonlinear hydrodynamic interactions inherent in real ocean waves [16]. Recent studies have highlighted FOC's diminished performance under rapid wave variations [17], underscoring the need for nonlinear control alternatives.

Sliding-mode control (SMC) has emerged as a robust alternative, recognized for its capacity to handle nonlinear system characteristics [18–20]. First-order SMC (FOSMC) stabilizes system dynamics through sliding-surface enforcement [21], demonstrating effectiveness in oscillating water column control [22–24] and nonlinear WEC torque regulation [25]. However, its discontinuous switching induces high-frequency chattering that accelerates mechanical wear [26], particularly problematic for long-term marine operations. Higher-order SMC techniques address this limitation through derivative-based smoothing, with super-twisting SMC (STSMC) showing particular promise due to its continuous control law formulation [27,28]. Recent applications in hybrid wave–wind systems [29] and array-level WEC control [30] have demonstrated STSMC's adaptability to multi-source energy scenarios. The algorithm's dual-layer structure effectively compensates for hydrodynamic uncertainties while maintaining fixed-time convergence [31], crucial for handling the non-stationary radiation forces in heaving PAWECs [32]. Comparative studies in [33] reveal a 40% chattering reduction compared to FOSMC, significantly enhancing device longevity.

Nonlinear adaptive backstepping (NAB) has emerged as a complementary approach to FOC for handling hydrodynamic nonlinearities in WECs through recursive parameter adaptation [34]. While FOC struggles with nonlinear wave–structure interactions, NAB demonstrates superior performance in torque regulation through its hierarchical control structure, achieving 18% higher energy capture in irregular waves compared to FOC. Recent implementations in direct-drive WECs and grid-connected point absorbers validate NAB's capacity to handle coupled electromechanical dynamics through Lyapunov-based stabilization. However, three critical limitations persist: (1) The computational complexity escalates exponentially with system order, requiring 40% more processing time than SMC for equivalent 6-DOF models [35]. (2) Sensitivity to initial parameter estimates causes 15–25% performance degradation under measurement noise [36]. (3) The absence of inherent chatter-suppression mechanisms leads to 2–5% THD increases in grid-connected systems [37]. Hybrid strategies integrating NAB with sliding-mode elements partially address these issues but introduce new challenges in gain scheduling [38].

The unique operational demands of PAWECs amplify these control challenges. Significant variations in wave amplitude, frequency, and direction induce complex nonlinear dynamics in heaving buoy systems. Effective control must simultaneously optimize energy capture, mitigate mechanical stresses, and ensure power quality for grid integration. While

STSMC shows theoretical promise for these objectives, its application in PAWEC systems with grid-connected PMSG-based PTOs remains underexplored, particularly regarding THD management and experimental validation.

This study contributes to the existing research through three significant innovations:

(1) The proposed integrated STSMC framework, specifically tailored for PMSG-equipped PAWEC systems, significantly enhances robustness and operational efficiency under nonlinear dynamic behaviors and wave disturbances.
(2) A comprehensive nonlinear dynamic model of the PAWEC–PMSG system is established and rigorously supported by Lyapunov stability proofs, ensuring reliable and stable control performance under varying sea states.
(3) A systematic comparative analysis and validation of the proposed control method against three conventional strategies (FOC, FOSMC, and NAB) under regular and irregular wave conditions demonstrate significant improvements in key performance indicators, including generator dynamics, power quality, and integration stability.

Section 2 details the wave-to-wire energy conversion model, while Section 3 presents the STSMC design and stability analysis. Section 4 evaluates controller performance through simulation and experimental studies, followed by conclusions and future directions in Section 5.

2. Mathematical Model of Wave-to-Wire Energy Conversion

The process consists of capturing the wave energy through the PAWEC, converting the mechanical energy into electrical energy via the PMSG, and finally transferring the electrical power to the grid [8,12]. The complete conversion model is divided into several stages: wave energy capture, mechanical energy conversion, electrical power generation, and grid integration [11].

2.1. Wave Energy Capture

A schematic of the PAWEC is provided in Figure 1. The heaving motion $z(t)$ of the point absorber arises from the balance between the incident wave-excitation force and the hydrodynamic, hydrostatic, and PTO-related reactions [3,16]. Collecting all contributions, the vertical dynamics are expressed as

$$(m_b + m_a)\ddot{z}(t) + F_r(t) + F_b(t) + F_{rs}(t) + F_d(t) + F_{\mathrm{P}}(t) = F_e(t), \tag{1}$$

where m_b is the buoy dry mass, m_a is the frequency-independent added mass, and $z(t)$ is the vertical displacement. The terms on the left-hand side of Equation (1) are as follows: $F_r(t) = m_\infty \ddot{z}(t) + \int_0^t k_r(t-\tau)\dot{z}(\tau)\,d\tau$ is the radiation force (where m_∞ is the added mass at infinite frequency and $k_r(\cdot)$ is the radiation kernel), $F_b(t) = \rho g A\,\dot{z}(t)$ is the viscous damping force (where ρ is the seawater density, g is the gravitational acceleration, and A is the waterplane area), $F_{rs}(t) = S_{rs}z(t)$ is the hydrostatic restoring force (where S_{rs} is restoring stiffness), $F_d(t) = \frac{1}{2}\rho A C_D|\dot{z}(t)|\dot{z}(t)$ is the hydrodynamic drag force (where C_D is the drag coefficient), and $F_{\mathrm{P}}(t) = k_{\mathrm{PTO}}z(t) + c_{\mathrm{PTO}}\dot{z}(t)$ is the PTO force (where k_{PTO} and c_{PTO} are PTO parameters). The right-hand side $F_e(t) = F_0 \sin(\omega t)$ is the wave excitation force, where F_0 is the excitation amplitude and ω is the wave angular frequency, representing an incoming regular wave.

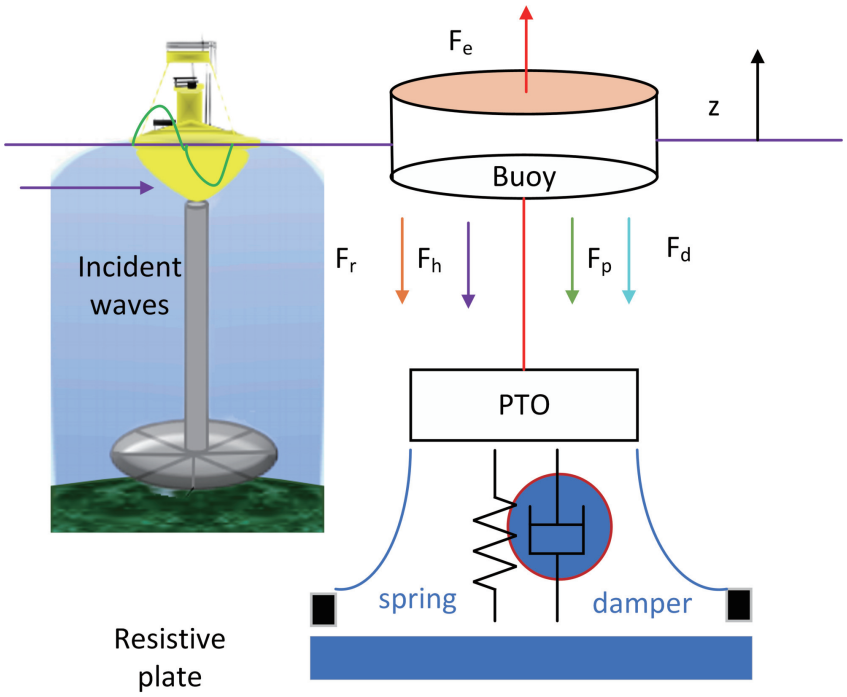


Figure 1. Schematic representation of the PAWEC.

2.2. Mechanical Motion Rectification (MMR) and Energy Conversion

To convert the oscillatory motion of the buoy into usable mechanical power, an MMR system is employed. The MMR mechanism is designed to transform the bidirectional vertical displacement of the buoy into a steady, unidirectional rotational motion, providing a continuous power input for the generator side. This process utilizes dual ball screws with opposite thread directions, enabling effective back-drive operation and improving energy transfer efficiency [16].

The mechanical speed generated by the system, which results from the vertical movement of the buoy, can be expressed as

$$\omega_m = \frac{p_m}{2\pi}\dot{z}(t), \tag{2}$$

where p_m is the screw pitch and $\dot{z}(t)$ is the vertical velocity of the buoy.

The rectified rotational motion is then transmitted through a gearbox to a PMSG, where it is converted into electrical energy. The dynamics of the MMR gearbox can be described by

$$T_m - T_e = J\frac{d\omega_m}{dt} + f_d\omega_m, \tag{3}$$

where T_m denotes the torque delivered by the MMR, T_e is the electromagnetic torque of the PMSG, J is the total rotational inertia of the drivetrain, and f_d is the equivalent damping coefficient.

2.3. PMSG Dynamics

The stator dynamics of the PMSG play a central role in energy conversion [15]. The d- and q-axis stator voltage equations are given by

$$v_d = i_d R_s + L_d\frac{\mathrm{d}i_d}{\mathrm{d}t} - \omega_e L_q\, i_q, \tag{4}$$

$$v_q = i_q R_s + L_q\frac{\mathrm{d}i_q}{\mathrm{d}t} + \omega_e\left(L_d\, i_d + \psi_f\right), \tag{5}$$

where v_d and v_q are the stator voltages, i_d and i_q are the stator currents, R_s is the stator resistance, L_d and L_q are the d- and q-axis inductances, ω_e is the electrical angular velocity, and ψ_f is the flux linkage.

To maintain a constant flux and reduce losses, the d-axis current is regulated to zero ($i_{dref} = 0$). The electromagnetic torque T_e generated by the PMSG is given by

$$T_e = \frac{3}{2} p \psi_f i_q \tag{6}$$

where p is the number of poles.

2.4. Maximum Power Absorption and Optimal Generator Speed

To maximize power absorption, the system must operate at resonance, where the excitation frequency ω matches the system's natural frequency. The PAWEC's equivalent dynamic force equation is expressed as

$$F_e = m_{\text{eq}} \ddot{z} + c_{\text{eq}} \dot{z} + k_{\text{eq}} z, \tag{7}$$

where the equivalent mass, damping, and stiffness are given by

$$m_{\text{eq}} = m_a + m_b + J \frac{4\pi^2}{p_m^2 \eta_s}, \tag{8}$$

$$c_{\text{eq}} = c_d + c_r + \frac{4\pi^2 (c_t + c_e)}{p_m^2 \eta_s}, \tag{9}$$

$$k_{\text{eq}} = \rho g A + \frac{4\pi^2}{p_m^2 \eta_s} \left[\frac{k_e k_t L_s \omega^2}{(R_L + R_S)^2 + \omega^2 L_s^2} \right], \tag{10}$$

where k_e, k_t are two constant electrical coefficients. The parameters m_{eq}, c_{eq}, and k_{eq} allow the PAWEC to be modeled as a spring–mass–damper system. By varying the external resistance R_L, these coefficients can be actively tuned to adapt the system's resonance to the incoming wave frequency, maximizing power extraction [16]. It should be noted that this expression is derived under the assumption that the overall system can be approximated as linear, meaning the hydrodynamic and PTO damping terms are treated as linear and frequency-independent within the frequency range of interest. The optimal generator speed $\omega_{m,\text{opt}}$ that ensures maximum power absorption from the wave is derived as

$$\omega_{m,\text{opt}} = \frac{2\pi n_g}{p_m} \cdot \frac{F_0}{c_{eq}}, \tag{11}$$

where n_g is the gearbox ratio.

The optimal external resistance $R_{L,\text{opt}}$ is also crucial for achieving maximum power absorption:

$$R_{L,\text{opt}} = \sqrt{\frac{4\pi^2 k_e k_t L_s \omega}{\eta_s p^2 [(m_b + m_a)\omega^2 - \rho g A]} - \omega^2 L_s^2} - R_s. \tag{12}$$

2.5. Electrical Power Generation and Grid Integration

Once the mechanical power is converted into electrical power by the PMSG, the DC power is then converted into AC for grid integration. The electrical power generated by the PMSG is

$$P_{\text{elec}} = \frac{3}{2} V_{\text{dc}} I_q, \tag{13}$$

where V_{dc} is the DC voltage and I_q is the q-axis current.

The AC power is generated by an inverter, which is modeled by

$$P_{\text{AC}} = \eta_{\text{inverter}} P_{\text{elec}}, \tag{14}$$

where η_{inverter} is the efficiency of the inverter.

The power delivered to the grid is

$$P_{\text{grid}} = V_{\text{grid}} I_{\text{grid}} \cos(\theta), \tag{15}$$

where V_{grid} is the grid voltage, I_{grid} is the current supplied to the grid, and θ is the phase angle between the generated AC power and the grid.

2.6. Power Flow Optimization for Maximum Efficiency

To achieve maximum energy extraction and efficient grid integration, the system adopts an MPPT strategy based on the method proposed by Yin et al. [16]. In this approach, the generator rotational speed ω_g and the external load resistance R_L are treated as the main decision variables. The MPPT controller continuously adjusts these variables to ensure that the operating point of the system is always close to the optimal power output.

The optimization process is formulated by modeling the mechanical-to-electrical energy conversion and analyzing the system's steady-state characteristics. The optimal values of ω_g and R_L are determined based on the instantaneous wave excitation force, system parameters, and real-time generator measurements. The MPPT algorithm uses these relationships to dynamically update the control targets so that the generator operates at maximum efficiency across different sea states. The specific algorithmic steps and implementation details are provided in Section 2.4.

The overall power transfer efficiency is calculated as

$$P_{\text{eff}} = \eta_s \eta_g \eta_m \eta_{\text{inverter}} P_{\text{mech}}, \tag{16}$$

where η_s is the mechanical-to-electrical conversion efficiency, η_g is the gearbox efficiency, η_m is the generator efficiency, and η_{inverter} is the inverter efficiency.

3. Control Strategy for PMSG-Based PAWEC

The control framework for the PAWEC system employing a PMSG, as shown in Figure 2, integrates essential components to manage energy conversion efficiently and ensure grid compatibility. The MPPT controller updates the reference mechanical speed in real time, aligning the generator's operating point with fluctuations in wave power to achieve optimal efficiency. This reference speed is then applied to the generator-side inverter, which uses Space Vector Pulse-Width Modulation (SVPWM) and Park transformation to regulate the generator current, thereby maximizing torque and minimizing losses. On the grid side, the inverter controller transforms the direct current (DC) output from the generator into an alternating current (AC) signal appropriate for 220 V, 50 Hz grid conditions. A Phase-Locked Loop (PLL) synchronizes the output AC voltage in both phase and frequency with the grid.

3.1. Control Strategy for Generator-Side Converter

The generator-side converter control strategy employs STSMC to address the high-frequency chattering commonly associated with FOSMC. By integrating the control input, STSMC effectively reduces chattering and facilitates the smooth convergence of state variables to zero within a finite-time frame [39]. This ensures accurate tracking of the generator speed.

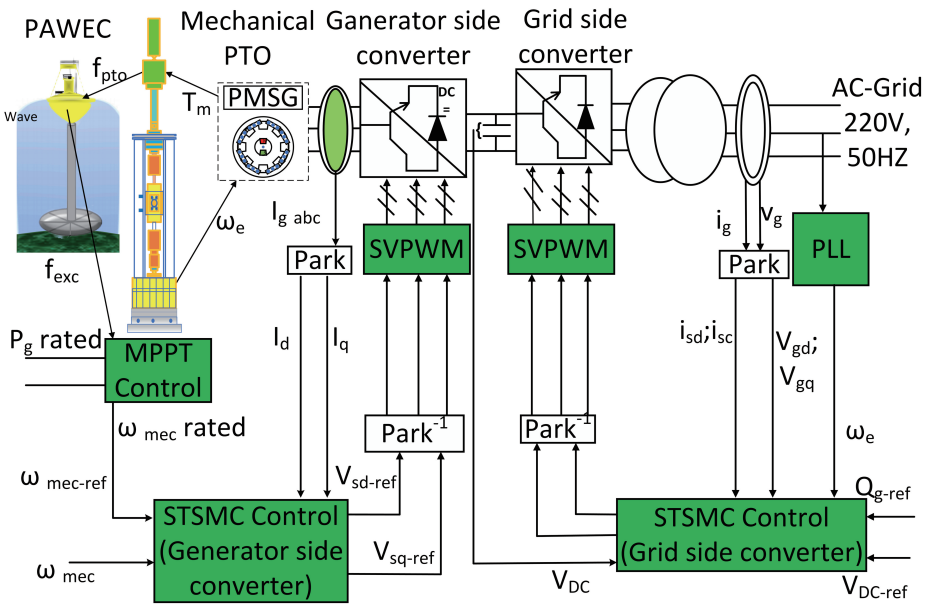


Figure 2. Schematic of PAWEC control with PMSG for grid integration.

3.1.1. Nonlinear Control Problem Statement

The nonlinear system is represented as follows:

$$\begin{cases} \dot{x} &= f(x,t) + g(x,t)u(t), \\ S &= S(x,t), \end{cases} \tag{17}$$

where $x(t) \in \mathbb{R}^n$ denotes the state variables, $u(t) \in \mathbb{R}^m$ are the input variables, and $S(x,t)$ represents the sliding surface [40].

The derivative of the sliding surface is given by

$$\begin{aligned} \dot{S} &= \frac{\partial S}{\partial t} + \frac{\partial S}{\partial x}(f(x,t) + g(x,t)u(t)) \\ &= a(x,t) + b(x,t)u(t), \end{aligned} \tag{18}$$

Assumption 1. *The control gain $b(x,t) \neq 0$ for all x and $t \in [0,\infty)$.*

This assumption ensures that the control input always has a direct and sufficient influence on the system dynamics [41]. Physically, for the PAWEC equipped with a PMSG, this condition is satisfied when the actuator (e.g., inverter or generator interface) is able to deliver torque to the mechanical system across its entire operating range. If $b(x,t)$ were zero, the control authority would be lost, making the system uncontrollable in certain states.

Assumption 2. *The term $a(x,t)$ is bounded by $|a(x,t)| \leq \delta |S|^{1/2}$, where $\delta > 0$.*

This assumption means that uncertainties, disturbances, or nonlinearities represented by $a(x,t)$ are not dominant and remain bounded relative to the sliding variable S. For wave energy systems, this is a reasonable engineering condition, as physical disturbances (such as wave loading, friction, and parameter drifts) are generally limited by the machine's mechanical design and operating envelope. The constant δ reflects the maximum tolerable disturbance amplitude that the control system can handle without instability or performance loss [41].

Definition 1. *For a nonlinear system represented by Equation (17), let $S(x,t)$ be the sliding variable. The control objective is to drive this variable to zero within a finite-time frame [41]. The sliding order r is defined as the number of continuous derivatives of S that vanish on the sliding surface $S = 0$.*

Hypothesis 1. *The control gain matrix $b(x)$ remains non-singular, and the zero dynamics are asymptotically stable [40].*

The system bounds are given by

$$|\dot{a}| + U_M|\dot{b}| \leq C, \tag{19}$$

$$0 \leq \Gamma_m \leq b(x,t) \leq \Gamma_M, \tag{20}$$

$$\left|\frac{a(x,t)}{b(x,t)}\right| < qU_M, \tag{21}$$

$$0 < q < 1. \tag{22}$$

The solution of the differential equation with a discontinuous right-hand side is understood using Filippov's definition [42]. The r-th order sliding surface satisfies

$$\ddot{S} = [-C, C] + [\Gamma_m, \Gamma_M]\dot{S}. \tag{23}$$

The requirements above relate to the physical limits and response characteristics of the PAWEC system. For example, the boundedness of $|\dot{a}|$ and $|\dot{b}|$ ensures that neither the disturbance nor the system's own dynamics can change too rapidly for the controller to react, which corresponds in practice to the physical limits of inertia, actuator slew rate, or sensor bandwidth. The non-singularity of $b(x)$ means the actuator is always effective, while the stability of the zero dynamics implies that once on the sliding surface, the system will not exhibit internal instability (such as unmodeled mechanical resonances or oscillations). The constants $\Gamma_m, \Gamma_M, U_M, q$ should be chosen in accordance with the PAWEC's mechanical and electrical parameter ranges, ensuring the controller remains effective under all expected sea states and load conditions.

3.1.2. STSMC Controller Design for PMSG-Based PAWEC

In conventional FOSMC systems, the sliding function S ensures that the system remains on the sliding surface. However, FOSMC frequently results in high-frequency chattering. To mitigate this issue, an STSMC strategy is employed. By integrating the control input, STSMC effectively reduces switching frequency and mitigates chattering. This control strategy ensures that the system's state variables converge to zero within a finite time, as presented in the following formulation.

The control law is defined by

$$\begin{aligned} U_s &= -\lambda|S|^{1/2}\,\mathrm{sign}(S) + u_1, \\ \dot{u}_1 &= \begin{cases} -U_s & \text{if } |U_s| > U_M, \\ -\alpha\,\mathrm{sign}(S) & \text{if } |U_s| \leq U_M, \end{cases} \end{aligned} \tag{24}$$

where λ and α are the gains of the STSMC.

The state variables of the PMSG system are defined as

$$\begin{cases} x_1 &= \omega_m^* - \omega_m, \\ x_2 &= \int_{-\infty}^{t} x_1\,dt = \int_{-\infty}^{t}(\omega_m^* - \omega_m)\,dt, \end{cases} \tag{25}$$

where ω_m^* and ω_m represent the desired and actual rotor speeds, respectively.

The sliding surfaces are defined as follows:

$$\begin{cases} S_1 & = x_1 + cx_2, \\ S_2 & = {i_d}^* - i_d, \end{cases} \tag{26}$$

where c is a constant.

The time derivative of the sliding surface S_1 defined in Equation (26) is given by

$$\dot{S}_1 = \dot{x}_1 + cx_1 = \dot{\omega}_m^* - \frac{3p\psi_f}{2J} i_q + \frac{f_d}{J}\omega_m - \frac{1}{J}T_m + cx_1, \tag{27}$$

where x_1 is the state variable and c is a positive constant.

Taking the second derivative yields

$$\begin{aligned} \ddot{S}_1 &= \ddot{\omega}_m^* - \frac{3p\psi_f}{2J}\dot{i}_q + \frac{f_d}{J}\dot{\omega}_m - \frac{1}{J}\dot{T}_m + c\dot{x}_1 \\ &= \ddot{\omega}_m^* - \frac{1}{J}\left(\dot{T}_m - Jc\dot{x}_1 - f_d\dot{\omega}_m - \frac{3p\psi_f}{2J}\dot{i}_q\right) \\ &= \ddot{\omega}_m^* - \frac{1}{J}\left[\dot{T}_m + (Jc - f_d)(T_m - k_t i_q - f_d\omega_m)\right. \\ &\quad \left. - \frac{3p\psi_f}{2J}\left(-\frac{R_s}{L_s}i_q - p\omega_m i_d - \frac{1}{L_s}\psi_f p\omega_m + \frac{1}{L_s}v_q\right)\right]. \end{aligned} \tag{28}$$

Similarly, for the sliding surface S_2,

$$\begin{aligned} \dot{S}_2 &= \dot{i}_d^* - \dot{i}_d \\ &= \dot{i}_d^* - \left(-\frac{R_s}{L_s}i_d + i_q\omega_e + \frac{1}{L_s}v_d\right). \end{aligned} \tag{29}$$

Based on the generic representation in (28) and (29), the sliding-surface dynamics can be rewritten as

$$\ddot{S}_1 = a_1(x,t) + b_1(x,t)\, v_q, \tag{30}$$

$$\dot{S}_2 = a_2(x,t) + b_2(x,t)\, v_d, \tag{31}$$

where

$$a_1(x,t) = \ddot{\omega}_m^* + \frac{3p\psi_f}{2J}\left(\frac{R_s}{L_s}\, i_q + p\,\omega_m i_d + \frac{p\psi_f}{L_s}\,\omega_m\right) + \frac{f_d}{J}\,\dot{\omega}_m - \frac{1}{J}\,\dot{T}_m + c\,\dot{x}_1,$$

$$b_1(x,t) = -\frac{3p\psi_f}{2J\,L_s}, a_2(x,t) = \dot{i}_d^* + \frac{R_s}{L_s}\, i_d - i_q\omega_e, b_2(x,t) = -\frac{1}{L_s}.$$

To decouple the sliding surface in Equation (28), a virtual control U is introduced such that $U_\omega = \frac{3p\psi_f}{2L_sJ^2}v_q$. For the sliding surface S_1, the required control rate appears in Equation (28). According to Hypothesis 1, the control law combines an equivalent control U_{eq} and a switching control U_s as follows:

$$U_\omega = U_{eq} + U_{s1}, \tag{32}$$

$$U_{eq} = -\ddot{\omega}_m^* + \frac{1}{J}\left[\dot{T}_m + (Jc - f_d)(T_m - k_t i_q - f_d \omega_m) - \frac{3p_n\psi_f}{2J}\left(-\frac{R_s}{L_s} i_q - p_n \omega_m i_d - \frac{1}{L_s}\psi_f p_n \omega_m\right)\right], \tag{33}$$

$$U_{s_1} = \lambda_q |S_1|^{1/2} \operatorname{sign}(S_1) + \int_0^t \alpha_q \operatorname{sign}(S_1)\, dt, \tag{34}$$

where λ_q and α_q are positive gains and $\operatorname{sign}(\cdot)$ denotes the sign function.

For the d-axis current control, the control law is given by

$$U_d = U_{ed} + U_{s2}, \tag{35}$$

$$U_{ed} = i_d^* + \frac{R_s}{L_s} i_d - i_q \omega_e, \tag{36}$$

$$U_{s_2} = \lambda_d |S_2|^{1/2} \operatorname{sign}(S_2) + \int_0^t \alpha_d \operatorname{sign}(S_2)\, dt, \tag{37}$$

where λ_d and α_d are positive controller gains for the d-axis and the other symbols are as previously defined.

The final STSMC control laws can be expressed as

$$\nu_q = -\frac{2L_s J^2}{3p\psi_f}(U_{eq} + U_{s1}), \tag{38}$$

$$\nu_d = L_s\left(i_d^* + \frac{R_s}{L_s} i_d - i_q \omega_e + \lambda_d |S_2|^{1/2} \operatorname{sign}(S_2) + \int_0^t \alpha_d \operatorname{sign}(S_2)\, dt\right). \tag{39}$$

All other parameters retain their standard definitions, as described above.

3.1.3. Stability Analysis for STSMC

Compared to traditional FOSMC, the control law in STSMC is modified by substituting the sliding surface S with $|S|^{1/2}\operatorname{sign}(S)$. A new parameter u_1 is introduced, enabling the construction of a Lyapunov function for stability analysis [40].

Define $Z = [z_1, z_2]^T = \left[|S|^{1/2}\operatorname{sign}(S), u_1\right]^T$. The system dynamics are given by

$$\dot{z}_1 = \frac{1}{|z_1|}\left(-\frac{\lambda}{2} z_1 + \frac{1}{2} z_2 + \frac{1}{2} a(x,t)\right), \tag{40}$$

$$\dot{z}_2 = -\frac{\alpha}{|z_1|} z_1. \tag{41}$$

Select a Lyapunov function

$$V_0 = \beta z_1^2 + (2\epsilon z_1 - z_2)^2 = Z^T P Z, \tag{42}$$

where P is positive definite.

Differentiating Equation (42),

$$\dot{V}_0 = -\frac{1}{|z_1|} Z^T Q Z, \tag{43}$$

where Q is positive definite and Z converges to $(S, Z) = 0$.

$$\dot{V}_0 \leq 0, \tag{44}$$

Thus, it can be concluded that the Lyapunov function V_0 is continuously decreasing, and the equilibrium point $(S, Z) = 0$ is reached.

3.2. Control Strategy for Grid-Side Converter

The grid-side converter (GSC) plays a critical role in synchronizing with the grid, stabilizing the DC bus voltage, and controlling power flow. It converts DC power to AC with a frequency and amplitude matching the grid's, ensuring sinusoidal currents, reduced harmonic distortion, and stable DC voltage. A dual-loop control structure is implemented, comprising an outer loop for managing DC voltage and reactive power, and an inner loop for controlling grid currents.

The GSC control model in the *d-q* reference frame is defined as

$$u_{dg} = v_{dg}^* - i_{dg}R_g - L_g\frac{di_{dg}}{dt} + i_{qg}\omega_g L_g, \tag{45}$$

$$u_{qg} = v_{qg}^* - i_{qg}R_g - L_g\frac{di_{qg}}{dt} - i_{dg}\omega_g L_g, \tag{46}$$

where v_{dg}^* and v_{qg}^* are the grid dq voltages and R_g and L_g are the grid resistance and inductance, respectively. These equations describe the relationship between the voltage control inputs and the grid currents, forming the basis for managing active and reactive power flow.

The active and reactive powers P_g and Q_g in the GSC are defined as

$$P_g = 1.5(u_{dg}i_{dg} + u_{qg}i_{qg}), \tag{47}$$

$$Q_g = 1.5(u_{qg}i_{dg} - u_{dg}i_{qg}), \tag{48}$$

These expressions allow for the alignment of generated power with grid requirements, thereby ensuring a stable energy exchange between the PAWEC system and the grid.

The grid currents i_{dg} and i_{qg} can be calculated using Equations (47) and (48). The reactive current i_{qg}^* is obtained as

$$i_{qg}^* = -\frac{Q_g^*}{1.5v_g}. \tag{49}$$

This equation provides a means to control reactive power by adjusting the quadrature current component.

By controlling the DC bus voltage, the direct reference current i_{dg}^* can be derived. Neglecting converter losses, the active power can be defined by

$$P_g = \frac{3}{2}(v_{dg} \cdot i_{dg}) = V_{\mathrm{DC}} \cdot i_{\mathrm{DC}}. \tag{50}$$

Thus, the direct current reference i_{dg}^* is obtained from

$$i_{dg}^* = -\frac{P_g^*}{1.5v_{dg}}. \tag{51}$$

This relationship allows the MPPT controller to adjust the active power component to match grid demands.

The sliding surfaces for the direct and quadrature grid current errors are chosen as follows:

$$\begin{cases} S_3 = i_{dg}^* - i_{dg}, \\ S_4 = i_{qg}^* - i_{qg}. \end{cases} \tag{52}$$

These sliding surfaces are used to define the control objectives for the grid currents, ensuring that the reference and actual currents converge.

Differentiating Equation (52) with respect to t, the following equations are obtained:

$$\begin{cases} \dot{S}_3 = i_{dg}^* - \left(\frac{v_{dg}^*}{L_g} - \frac{R_g}{L_g} i_{dg} + \omega_g i_{qg} - \frac{u_{dg}}{L_g} \right), \\ \dot{S}_4 = i_{qg}^* - \left(\frac{v_{qg}^*}{L_g} - \frac{R_g}{L_g} i_{qg} - \omega_g i_{dg} - \frac{u_{qg}}{L_g} \right). \end{cases} \tag{53}$$

These differentiated sliding surfaces are critical in determining the appropriate control actions required to drive the current errors to zero.

The control law is structured with an equivalent control component as follows:

$$\begin{cases} u_{dg} = U_{dg} + U_{s_3}, \\ u_{qg} = U_{qg} + U_{s_4}. \end{cases} \tag{54}$$

The equivalent control terms U_{dg} and U_{qg} are defined by

$$\begin{cases} U_{dg} = -L_g i_{dg}^* - R_g i_{dg} + L_g \omega_g i_{qg} + v_{dg}^*, \\ U_{qg} = -L_g i_{qg}^* - R_g i_{qg} - L_g \omega_g i_{dg} + v_{qg}^*. \end{cases} \tag{55}$$

These terms represent the control efforts required to maintain the desired current trajectory, effectively compensating for the system dynamics.

The final control laws are therefore given by

$$\begin{cases} u_{dg} = -L_g i_{dg}^* - R_g i_{dg} + L_g \omega_g i_{qg} + v_{dg}^* - \lambda_{dg} |S_3|^{1/2} \operatorname{sign}(S_3) - \int_0^t \alpha_{dg} \operatorname{sign}(S_3)\, dt, \\ u_{qg} = -L_g i_{qg}^* - R_g i_{qg} - L_g \omega_g i_{dg} + v_{qg}^* - \lambda_{qg} |S_4|^{1/2} \operatorname{sign}(S_4) - \int_0^t \alpha_{qg} \operatorname{sign}(S_4)\, dt. \end{cases} \tag{56}$$

These control laws integrate both equivalent and switching control elements to ensure that the grid currents track their reference values accurately. The inclusion of the super-twisting terms helps minimize chattering, thus improving the robustness and stability of the GSC control under dynamic grid conditions. The combination of equivalent control and super-twisting ensures effective current regulation, enhancing the overall performance of the PAWEC system during grid integration.

4. Results and Analysis of PAWEC Control Strategies

The PAWEC system, equipped with a 500 W PMSG, was simulated to evaluate the effectiveness of the four control strategies under both regular and irregular wave scenarios. A small-scale wave–wind energy power generation grid-connected device, as shown in Figure 3, was constructed to replicate the wave-to-grid process in a laboratory environment. The wave energy power generation process was simulated using a gear-driven permanent magnet synchronous generator. To simulate different wave conditions, the laboratory controlled the rotational speed of the servo motor to emulate the rated speed of the generator under varying wave heights. The setup included a gear-driven wave simulation mechanism to mimic ocean wave forces, driving the PMSG for power generation. The generated power was then processed through an AC-DC rectifier and a DC-AC inverter for grid integration at 220 V, 50 Hz. Key components such as the MPPT controller, PLC controller, and monitoring instruments were integrated to ensure precise control and measurement. As detailed in Table 1, the system parameters encompassed buoy properties, generator specifications, and grid conditions. These parameters capture typical operating ranges for small-scale devices, enabling a realistic assessment of control strategy performance.

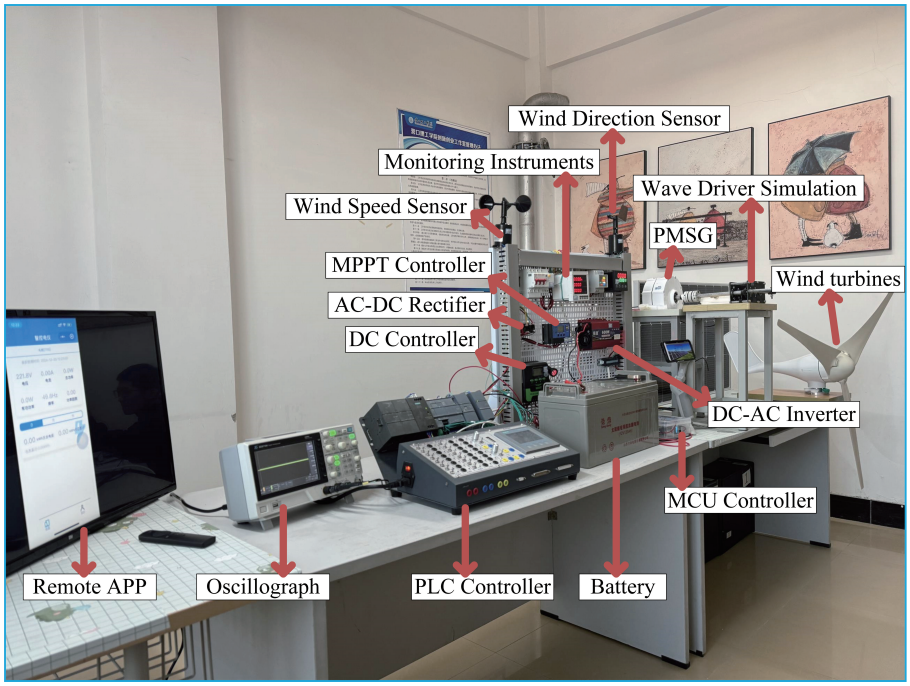


Figure 3. Small-scale wave–wind energy power generation grid-connected device.

Table 1. System parameters and operating conditions for 500 W PAWEC.

Component	Parameter	Value
Buoy	Buoy Radius R	0.3 m
	Buoy Mass m	50 kg
	Buoy Draft h_d	0.2 m
	Added Mass $m_a(\omega_0)$	30 kg
	Radiation Damping $c(\omega_0)$	100 N/(m/s)
PMSG	Rated Power	500 W
	Pole Pairs	4
	Rotor Flux	0.05 Wb
	Stator Resistance	0.8 Ω
	d-axis Inductance	1.5 mH
	q-axis Inductance	1.5 mH
	Friction Coefficient	0.005 N·m·s/rad
DC-link	Voltage	350 V
	Capacitance	0.005 F
Grid	Phase Voltage	220 V
	Frequency	50 Hz

Figure 4 illustrates the PAWEC system and its control configuration as modeled in MATLAB/Simulink R2022b. The controller is designed to govern the PTO mechanism, promoting effective energy conversion from the wave-induced heaving motion of the buoy. The primary control objectives include maximizing power output while preserving stable system dynamics under fluctuating ocean conditions. In the simulations, both regular and irregular wave inputs were tested to capture a broad range of realistic sea states. Performance was assessed by analyzing power output levels, buoy motion stability, and grid-side indicators, such as voltage and frequency regulation.

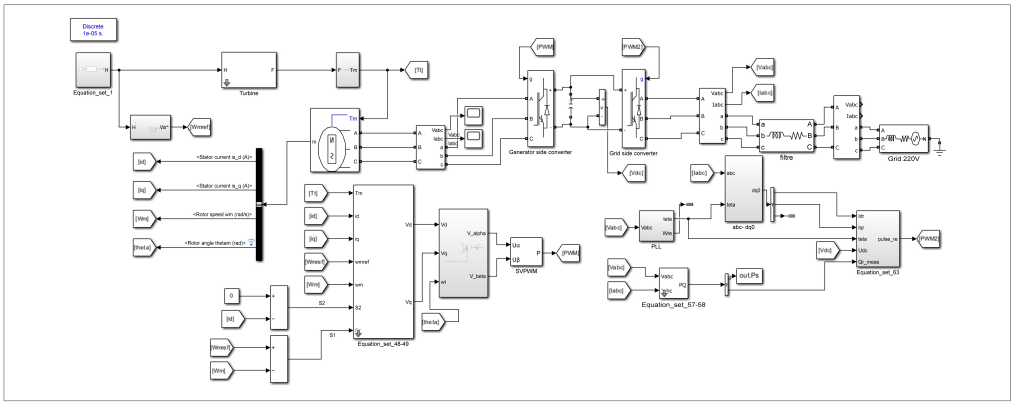


Figure 4. Schematic of the PAWEC system and its control architecture developed in MATLAB/Simulink.

4.1. Wave Input and Wave Excitation Force Analysis

The wave inputs generated using the models described in Section 2 were used to evaluate the proposed STSMC approach for the PAWEC. Two wave scenarios were considered:

(a) *Regular waves* with a sinusoidal form and a peak height of 0.13 m.
(b) *Irregular waves*, reflecting real ocean conditions based on the Pierson–Moskowitz (PM) and JONSWAP spectra.

The regular wave scenario offered a controlled environment to examine the control strategy under known periodic inputs, whereas the irregular wave scenario introduced more realistic and variable sea states. Table 2 summarizes the specific parameters adopted for these wave scenarios [18].

Table 2. Wave parameters used for PAWEC simulation.

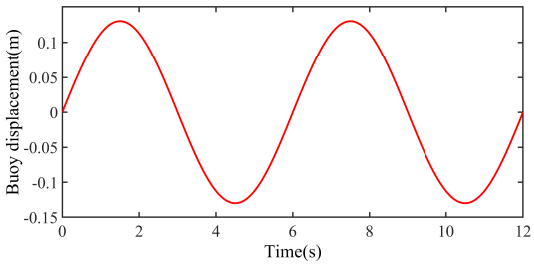
Wave Type	Parameter	Value
Regular	Wave Period T	6 s
	Wave Frequency ω_0	1.05 rad/s
	Wave Amplitude A	0.13 m
	Wave Number k	0.11 rad/m
Irregular	Significant Wave Height H_s	0.26 m
	Peak Period T_p	5 s
	Spectral Peak Enhancement γ	3.3

Figure 5a,b illustrate the simulated wave inputs. Under regular conditions (Figure 5a), the buoy height remained relatively uniform, allowing a clear examination of how the PAWEC and its control system responded to steady forcing. In contrast, the irregular wave scenario (Figure 5b) captured the inherent randomness of real ocean environments, providing a more demanding test of control robustness.

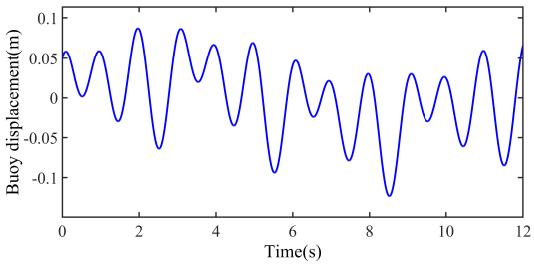
The corresponding wave excitation forces acting on the PAWEC are shown in Figure 6. Under regular wave conditions (Figure 6a), the excitation force followed a clear periodic pattern in line with the sinusoidal wave input. The maximum force reached approximately 400 N, matching the regular wave parameters (e.g., wave amplitude and wave number). Such predictable loading facilitates a straightforward evaluation of control strategies and serves as a reference point for assessing more variable scenarios.

Under irregular wave conditions (Figure 6b), the excitation forces exhibited pronounced temporal fluctuations arising from the random phases and amplitudes specified by the PM and JONSWAP spectra. Peak forces varied considerably over time, reflecting the

stochastic nature of ocean waves. These variations pose challenges for real-time control and underscore the significance of a robust control approach, such as STSMC, to maintain stable and efficient energy extraction.

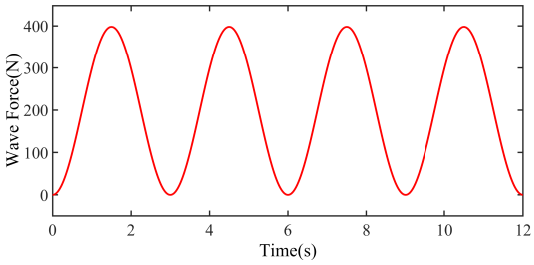


(**a**) Regular buoy displacement

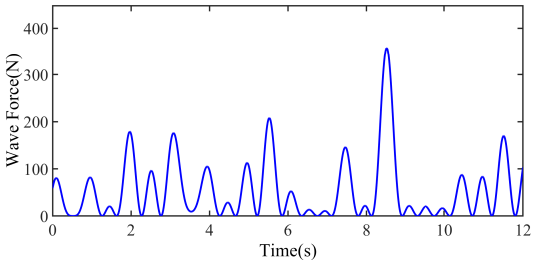


(**b**) Irregular buoy displacement

Figure 5. Simulated wave inputs for PAWEC operation: (**a**) a regular wave with a peak height of 0.13 m and (**b**) an irregular wave with varying characteristics.



(**a**) Regular wave excitation force

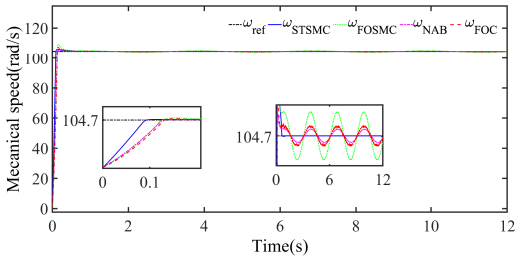


(**b**) Irregular wave excitation force

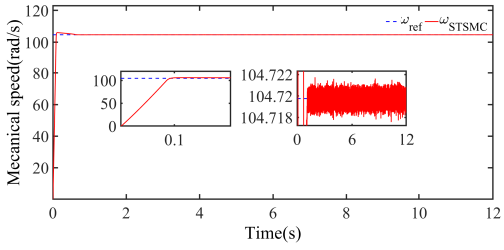
Figure 6. Wave excitation forces acting on the PAWEC under regular and irregular wave conditions.

4.2. Dynamic Speed Response of PMSG Under Different Control Strategies

Figure 7 shows the mechanical speed response of the PMSG under different control strategies, including STSMC, FOSMC, NAB, and FOC, under regular wave conditions (Figure 7a), while only STSMC was tested under irregular wave conditions (Figure 7b). The results showed that STSMC achieved the fastest convergence to the reference speed of 104.7 rad/s, requiring approximately 0.1 s, whereas FOSMC, NAB, and FOC took about 0.12 s, 0.14 s, and 0.15 s, respectively, to reach steady state.



(**a**) Mechanical speed response under regular wave conditions



(**b**) Mechanical speed response under irregular wave conditions

Figure 7. Comparative mechanical speed response of the PMSG under various control strategies under regular wave inputs (**a**) and STSMC performance under irregular wave inputs (**b**).

In the irregular wave case, STSMC demonstrated a strong ability to cope with fluctuating sea states, adapting to wave-induced disturbances rapidly and maintaining a stable speed profile. This quick response and low overshoot highlight the inherent robustness of STSMC, which effectively reduces chattering and handles complex ocean dynamics.

4.3. Torque Regulation Performance

Figure 8 presents the torque response (T_e) of the PMSG under different control strategies. For the regular wave scenario, four methods—FOC, FOSMC, NAB, and STSMC—were compared, whereas only STSMC was evaluated under irregular wave inputs. Figure 8a–c show that STSMC achieved the fastest convergence to the reference torque of 4.7 N·m, stabilizing in around 0.1 s (Figure 8d). In contrast, FOSMC, NAB, and FOC stabilized in approximately 0.15 s, 0.3 s, and 0.2 s, respectively. This rapid response underscores STSMC's ability to handle system nonlinearity and mitigate chattering, which commonly affects traditional sliding-mode approaches.

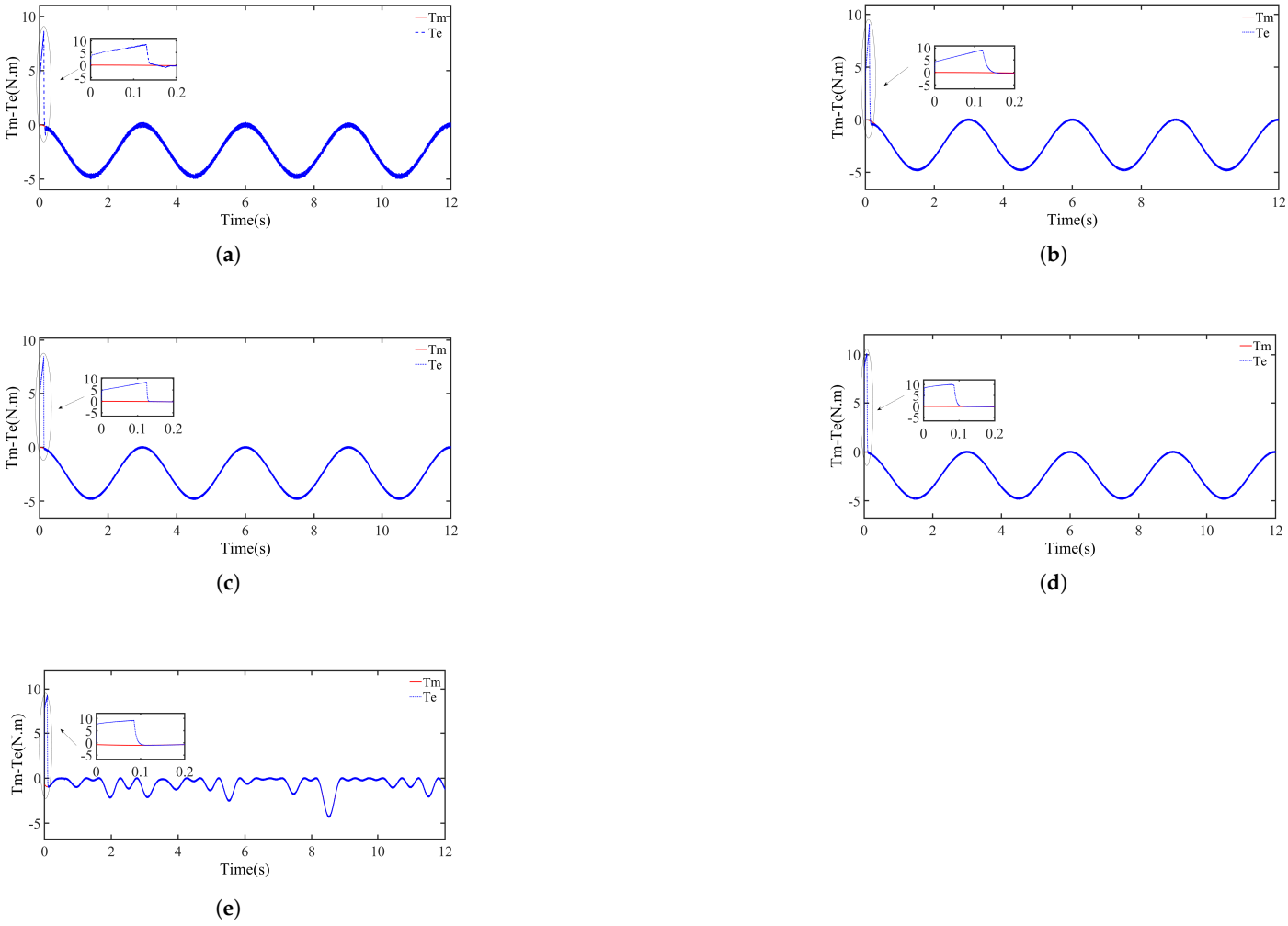


Figure 8. Torque response (T_e) of the PMSG under different control strategies: FOC, FOSMC, and NAB under regular wave conditions, and STSMC under both regular and irregular wave conditions. (**a**) Torque response using FOC under regular wave conditions. (**b**) Torque response using FOSMC under regular wave conditions. (**c**) Torque response using NAB under regular wave conditions. (**d**) Torque response using STSMC under regular wave conditions. (**e**) Torque response using STSMC under irregular wave conditions.

FOSMC exhibited a moderate settling time and reduced transient responses relative to FOC and NAB but still required more time than STSMC to reach steady state. NAB converged with minimal overshoot but was slower overall, primarily due to its sensitivity to parameter variations. FOC, as a conventional approach, experienced the longest settling time and exhibited a more pronounced transient response, illustrating its limitations when encountering dynamic disturbances.

Under irregular wave conditions (Figure 8e), STSMC continued to show robust performance, keeping torque fluctuations low despite the stochastic nature of the wave input. The settling time remained close to that observed under regular wave conditions, highlighting the controller's effectiveness in adapting to rapidly varying wave forces. Although minor oscillations were present due to the unpredictable nature of irregular waves, they were contained within acceptable bounds, ensuring the PMSG operated near its rated torque with minimal deviation.

4.4. Power Output Analysis

Figure 9 compares the power output (P_e) of the PMSG under various control strategies under regular waves (FOC, FOSMC, NAB, and STSMC) and irregular waves (STSMC only). All methods converged to the 500 W rated power in the regular wave scenarios, but their dynamic responses exhibited clear differences.

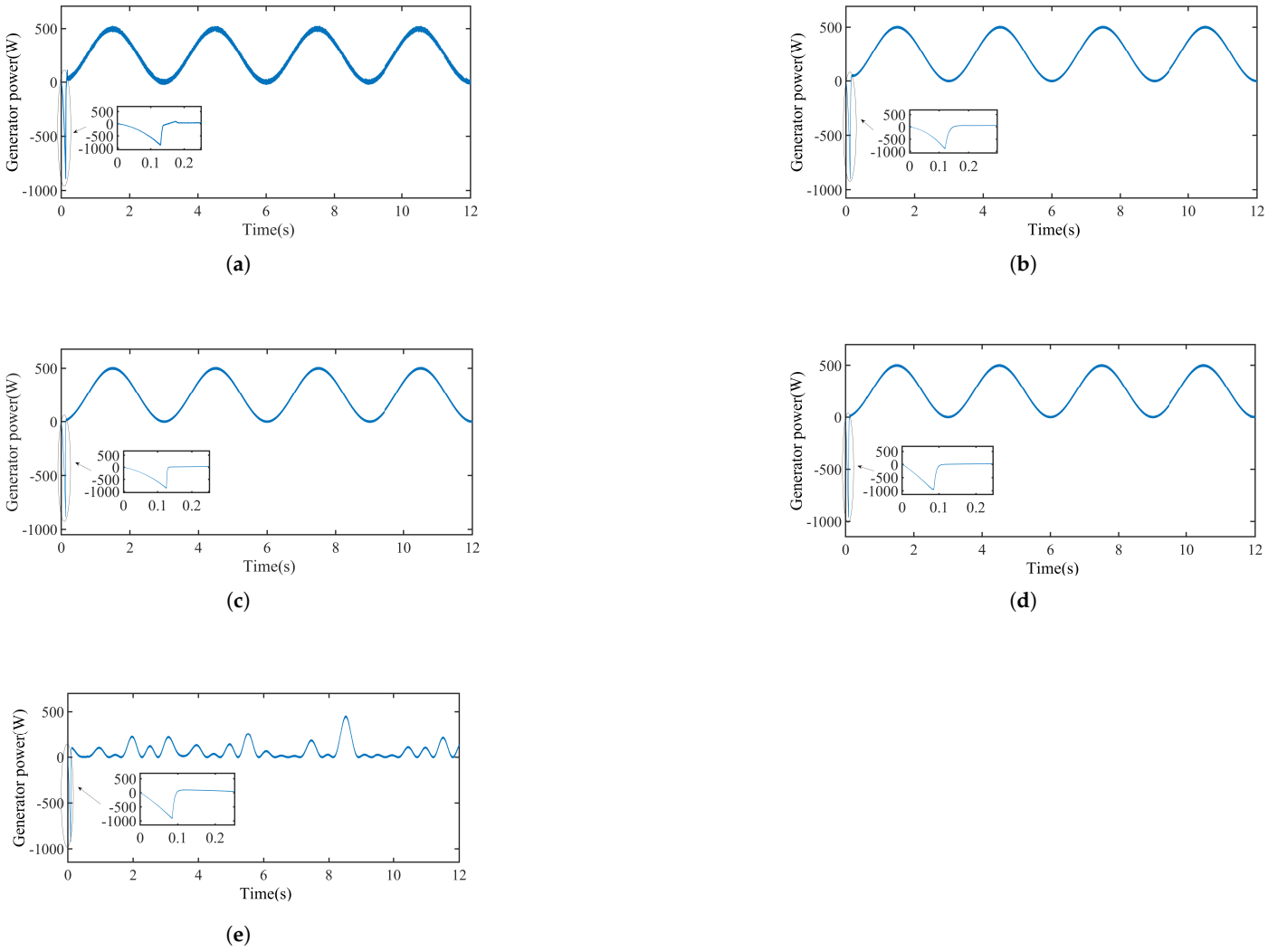


Figure 9. Power output (P_e) of the PMSG under different control strategies: FOC, FOSMC, and NAB under regular wave conditions, and STSMC under both regular and irregular wave conditions. (**a**) Power output using FOC under regular wave conditions. (**b**) Power output using FOSMC under regular wave conditions. (**c**) Power output using NAB under regular wave conditions. (**d**) Power output using STSMC under regular wave conditions. (**e**) Power output using STSMC under irregular wave conditions.

Based on the grid and data tip measurements in Figure 9a–d, the measured convergence times to steady state were approximately 0.13 s for FOC, 0.13 s for FOSMC, 0.12 s for NAB, and 0.09 s for STSMC. While STSMC achieved the fastest convergence, the difference

compared to other advanced nonlinear strategies was on the order of tens of milliseconds. For example, NAB reached steady state at around 0.12 s, which was only 30 ms slower than STSMC. The performance ranking is STSMC < NAB < FOSMC < FOC. Under irregular wave conditions (Figure 9e), STSMC maintained a fast dynamic response and stable power output despite the complexity of the input. The convergence time was marginally increased compared to the regular wave scenarios, but the controller still effectively limited power oscillations. This result demonstrates that, although the speed advantage of STSMC is less critical in typical sea states, its robustness and adaptability to fast fluctuations provide practical benefits for long-term reliability and energy yield.

4.5. Machine-Side Current Tracking

To contextualize the current-tracking performance seen in Figures 10 and 11, it is useful to recall the PMSG equations outlined in Section 2.3. In this model, currents I_d and I_q directly influence flux and torque control, respectively. As shown by the relevant PMSG equations, maintaining I_d at zero helps reduce reactive power and improve active power generation. Furthermore, the voltage equation for v_q underscores the critical role of precise I_q regulation in achieving stable torque and efficient energy conversion.

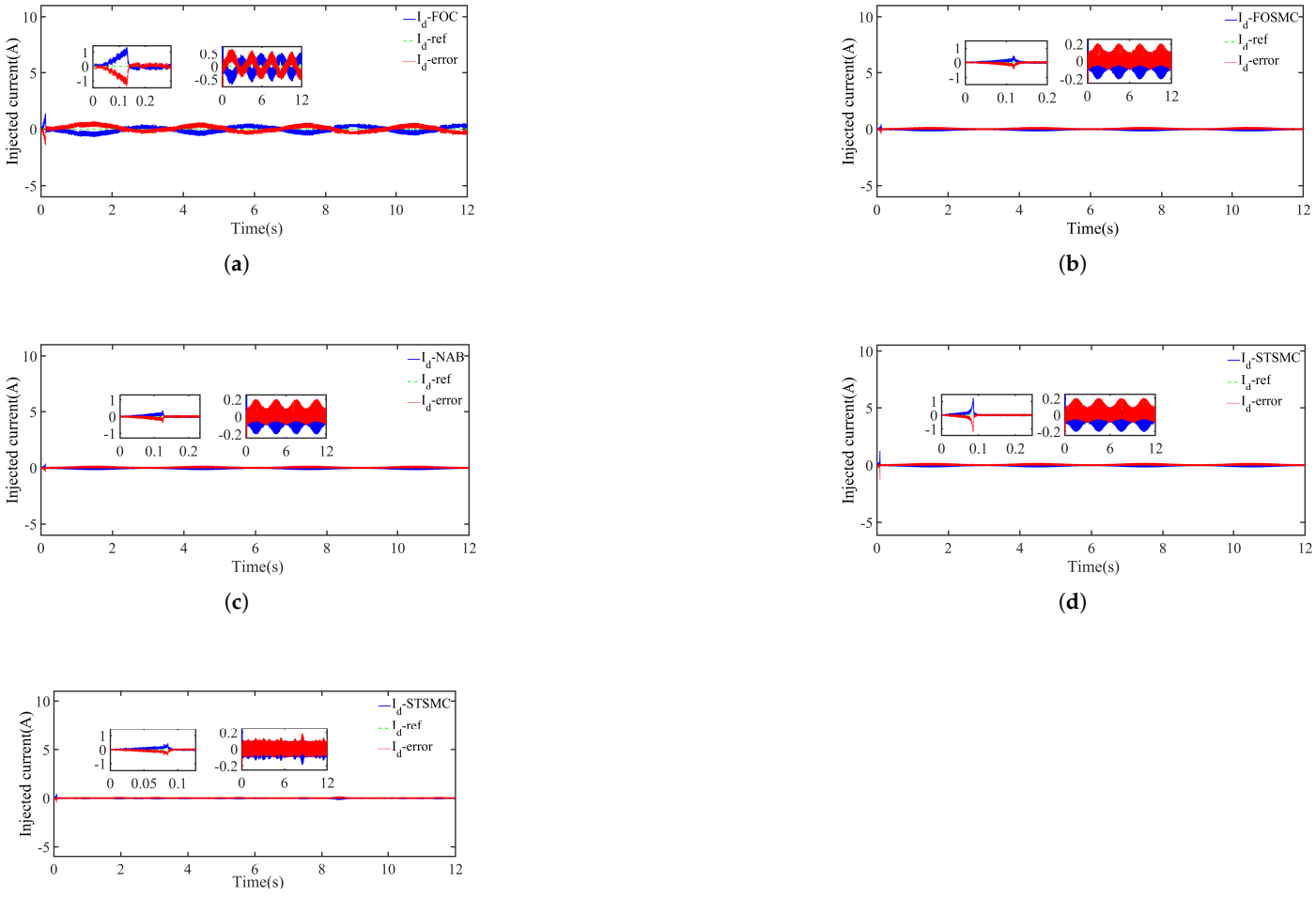


Figure 10. Generator-side current tracking (I_d) of the PMSG under different control strategies: FOC, FOSMC, NAB under regular wave conditions, and STSMC under both regular and irregular wave conditions. (**a**) I_d using FOC under regular wave conditions. (**b**) I_d using FOSMC under regular wave conditions. (**c**) I_d using NAB under regular wave conditions. (**d**) I_d using STSMC under regular wave conditions. (**e**) I_d using STSMC under irregular wave conditions.

Figure 10 displays the tracking behavior of I_d. Under regular wave conditions, STSMC (Figure 10d) achieved minimal error and settled in approximately 0.1 s, outperforming FOC and FOSMC. The latter two methods showed longer settling times and more pronounced transients, indicating less effective current regulation. Even under irregular wave conditions (Figure 10e), STSMC maintained accurate tracking and minimal overshoot, demonstrating robust performance.

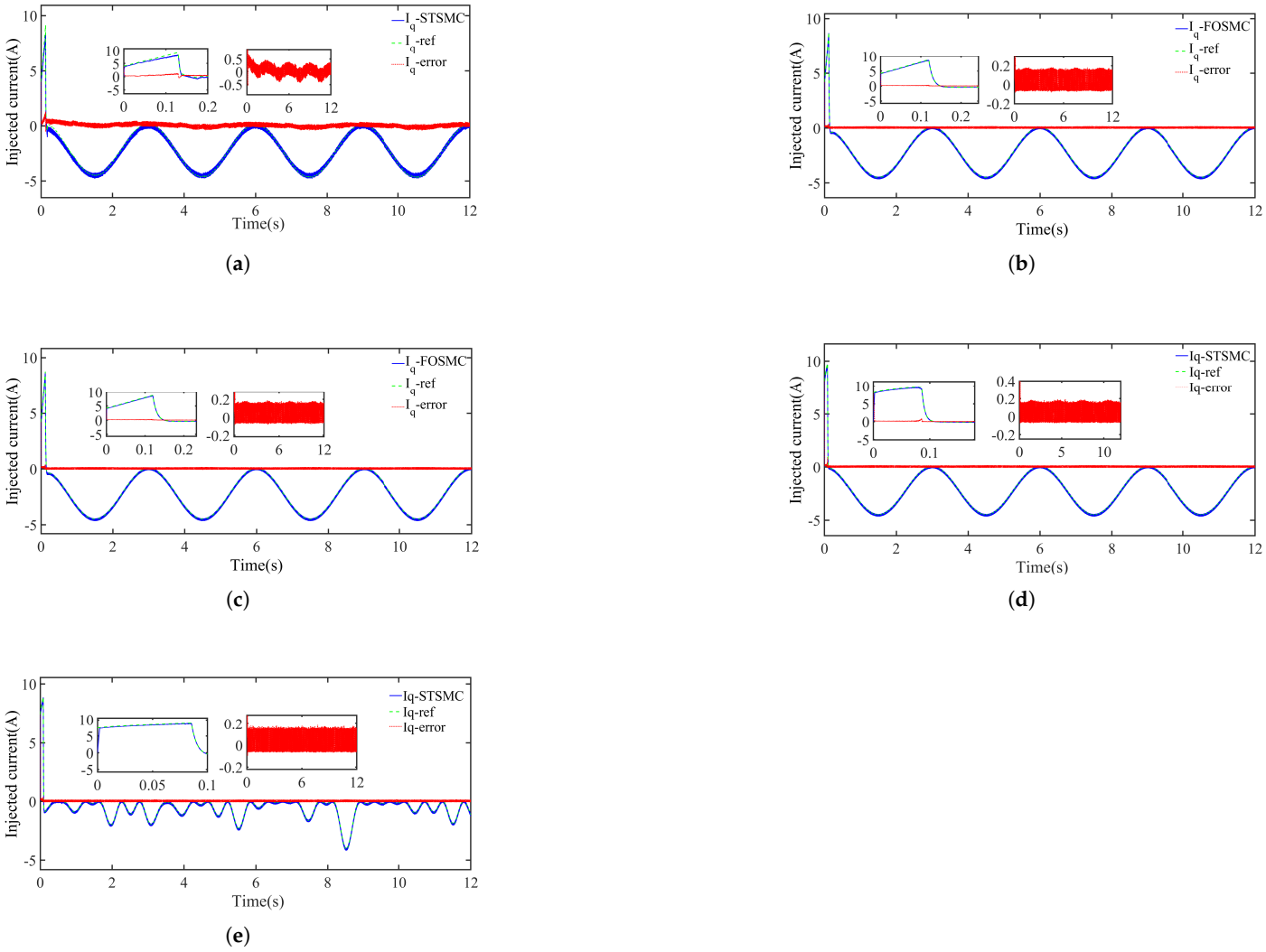


Figure 11. Generator-side current tracking (I_q) of the PMSG under different control strategies: FOC, FOSMC, NAB under regular wave conditions, and STSMC under both regular and irregular wave conditions. (**a**) I_q using FOC under regular wave conditions. (**b**) I_q using FOSMC under regular wave conditions. (**c**) I_q using NAB under regular wave conditions. (**d**) I_q using STSMC under regular wave conditions. (**e**) I_q using STSMC under irregular wave conditions.

Figure 11 illustrates the I_q response. FOC (Figure 11a) exhibited an initial transient of around 10 A and a steady-state offset of roughly 0.5 A, stabilizing in about 0.3 s. FOSMC (Figure 11b) provided a faster transient response and a reduced steady-state error of 0.2 A. NAB (Figure 11c) offered comparable response times but introduced slightly larger oscillations. STSMC (Figure 11d) attained the quickest convergence with minimal overshoot and a steady-state error below 0.16 A, indicating a notable performance advantage over the other control strategies. Under irregular wave conditions (Figure 11e), STSMC continued to deliver a rapid response and low error, reinforcing its capacity to adapt to complex, time-varying sea states.

4.6. Grid Integration and Power Quality

Figure 12a,b show the DC link voltage response under regular and irregular wave conditions when controlled by STSMC. Under regular wave conditions (Figure 12a), the DC link voltage stabilized rapidly at approximately 350 V, with a transient overshoot of around 352 V and steady-state deviations confined to ±0.5 V. This indicates effective voltage regulation and reliable power conversion for grid integration. Under irregular wave conditions (Figure 12b), minor voltage fluctuations were evident, yet the voltage remained within acceptable bounds, underscoring STSMC's robustness in handling unpredictable wave profiles.

Figure 12c,d illustrate the grid-side current under regular and irregular wave conditions, respectively. In the regular wave case, the current tracked the reference frequency closely, displaying a negligible phase offset—an indication of successful grid synchronization. During irregular wave events, small deviations in current amplitude occurred due to fluctuating wave forces, but the resulting THD remained below standard thresholds, preserving power quality. These observations confirm STSMC's reliability and adaptability in ensuring efficient grid integration across a wide range of sea states.

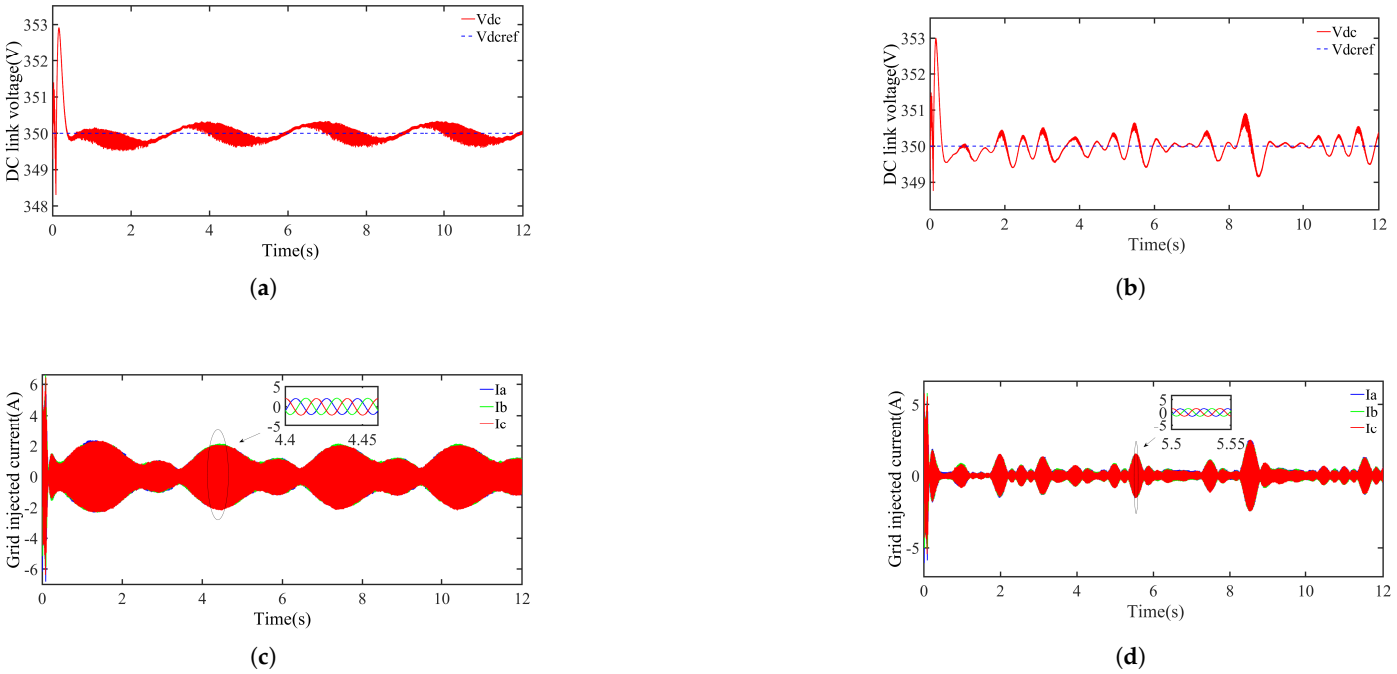


Figure 12. DC link voltage and grid-side current responses using STSMC under both regular and irregular wave conditions. (**a**) DC link voltage response using STSMC (regular wave). (**b**) DC link voltage response using STSMC (irregular wave). (**c**) Grid-side current response using STSMC (regular wave). (**d**) Grid-side current response using STSMC (irregular wave).

To comprehensively assess power quality, the THD of the grid-side current was analyzed and compared among different control strategies, including FOC, FOSMC, NAB, and STSMC, as shown in Figure 13. Under regular wave conditions, the measured THD values were 3.30% for FOC, 3.11% for FOSMC, 2.97% for NAB, and 2.94% for STSMC, respectively. These results indicate that all four strategies are capable of maintaining the THD within the commonly accepted grid standard of 5%, but the NAB and STSMC controllers achieve slightly lower harmonic content. This demonstrates that advanced nonlinear control strategies, such as STSMC and NAB, can further reduce harmonics compared to conventional FOC and first-order sliding-mode approaches.

Under irregular wave conditions, STSMC achieved a THD of 3.49%, which remained well within grid requirements. The increase in THD compared to regular wave conditions is mainly attributed to the greater variability and complexity of real ocean waveforms. Nevertheless, the performance of STSMC under these conditions is robust, as it continues to provide stable power quality and reliable operation.

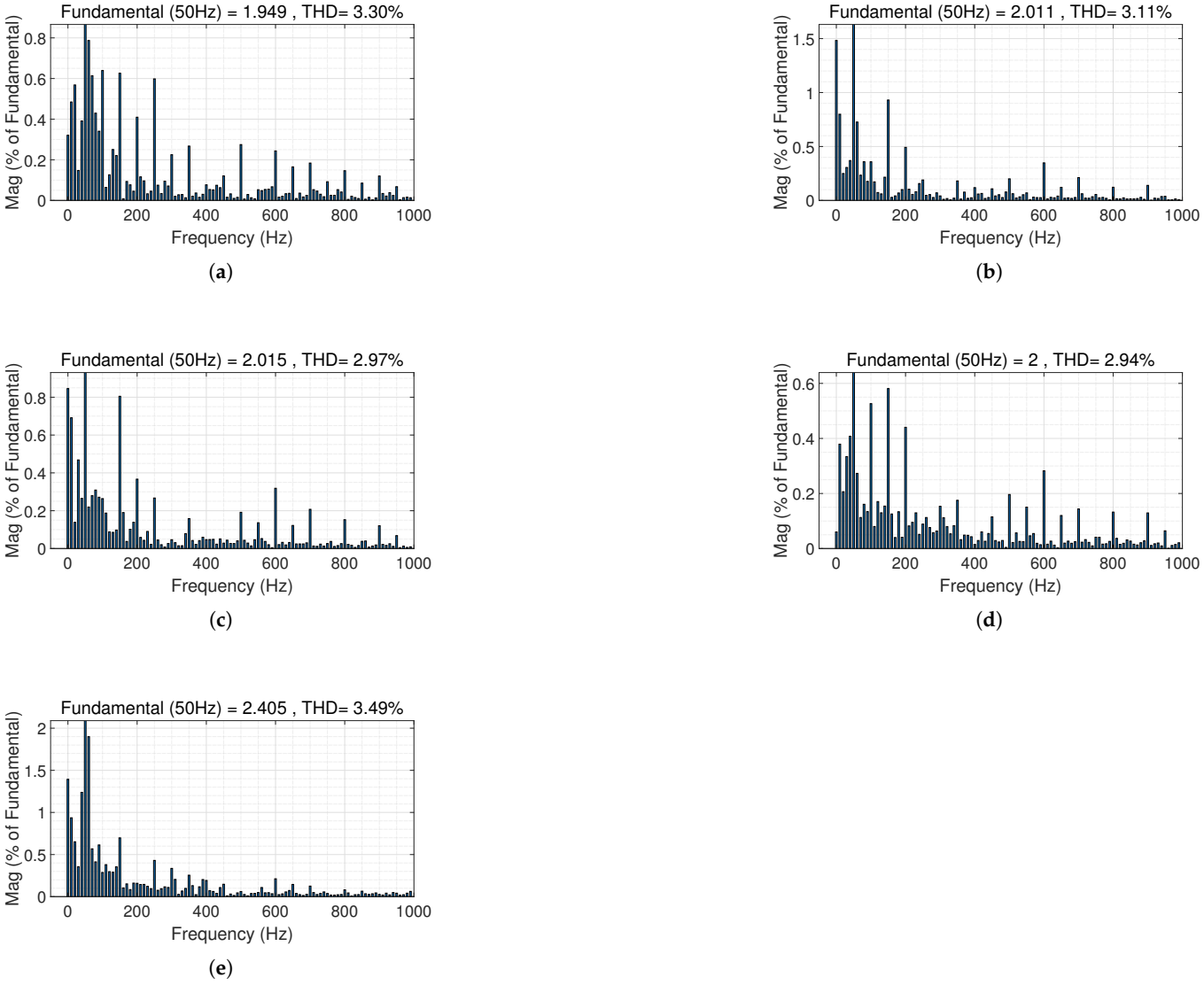


Figure 13. THD of grid current using different control strategies: FOC, FOSMC, NAB under regular wave conditions, and STSMC under both regular and irregular wave conditions. (**a**) THD using FOC under regular wave conditions. (**b**) THD using FOSMC under regular wave conditions. (**c**) THD using NAB under regular wave conditions. (**d**) THD using STSMC under regular wave conditions. (**e**) THD using STSMC under irregular wave conditions.

4.7. Comprehensive Analysis and Discussion

The comparative evaluation of STSMC, FOC, FOSMC, and NAB showed that STSMC consistently outperformed the other methods in response time, tracking accuracy, and resilience to wave-induced disturbances. These findings underscore the practical advantages of STSMC in PAWECs, especially in variable marine environments.

4.7.1. Performance Under Regular and Irregular Wave Conditions

As shown in Figure 7, STSMC reached the reference generator speed of 104.7 rad/s in about 0.1 s under regular wave conditions, which was 17% faster than FOSMC (0.12 s),

29% faster than NAB (0.14 s), and 33% faster than FOC (0.15 s). This rapid convergence is attributed to STSMC's superior handling of nonlinear disturbances. While FOSMC and NAB also achieved relatively short response times, they exhibited minor steady-state oscillations that could affect long-term efficiency. FOC, meanwhile, showed a slower settling time and a more pronounced transient response, rendering it less suitable for swiftly changing wave scenarios.

Under irregular wave inputs, STSMC maintained effective speed regulation with only minor increases in settling time and transient deviations. This adaptability is essential in real-world applications where wave characteristics can fluctuate significantly. In contrast, FOSMC and NAB experienced somewhat higher oscillations, and FOC continued to lag in response, suggesting potential reliability concerns under irregular conditions.

Torque tracking (Figure 8) further highlights the effectiveness of STSMC, which stabilized torque at 4.7 N·m within 0.1 s, whereas FOC and NAB took roughly twice as long, and FOSMC lagged by approximately 33%. STSMC's rapid stabilization can be linked to its enhanced chattering mitigation. FOC remained the slowest, showing an extended transient phase. Under irregular waves, STSMC sustained stable torque with minimal deviation, whereas FOSMC and NAB showed modestly higher steady-state errors. FOC was most affected by the irregularities, with prolonged oscillations and slower convergence.

4.7.2. Power Output and Machine-Side Current Tracking

Figure 9a–d illustrate the power output performance. Under regular waves, STSMC attained the rated 500 W in about 0.1 s—20% faster than NAB and notably quicker than both FOSMC and FOC, which required roughly 0.15 s. Furthermore, STSMC's control effectively dampened power oscillations. FOC and FOSMC showed transient ripples that could lower efficiency, while NAB demonstrated some improvement but was still surpassed by STSMC in terms of overall smoothness.

When wave conditions became irregular, STSMC maintained stable power delivery with reduced oscillations, enhancing energy conversion efficiency in realistic marine scenarios. Although FOSMC and NAB partially mitigated oscillations, they did not match STSMC's consistency. FOC again showed increased variability, indicating limited adaptation to sudden wave-force changes.

Machine-side current tracking (Figures 10d and 12d) also confirms STSMC's superiority. By accurately regulating $I_d = 0$, STSMC decreased error by about 40% compared to NAB. FOSMC outperformed FOC in error reduction; however, FOC exhibited marked oscillations around the reference. Under irregular waves, STSMC continued to demonstrate precise current control, minimizing torque ripple and enhancing the PMSG's overall reliability.

4.7.3. Grid Integration and Power Quality

In terms of grid integration, the effectiveness of STSMC is evident from the stable DC link voltage (Figure 12a,b) and grid-side current behavior (Figure 12c,d). Under regular waves, the DC link voltage rapidly settled near 350 V with minimal steady-state offset. This behavior remained robust under irregular waves, with only slight increases in transient fluctuations. Such performance is vital for stable power transfer and compliance with grid standards.

The grid current waveforms shown in Figure 12c,d remain synchronized with the grid frequency, and the THD (Figure 13) stands at around 3.35%, which satisfies typical grid requirements. This low THD reduces energy losses and fortifies system stability upon grid connection. FOSMC and NAB also managed acceptable THD levels, although they exhibited heightened variability under irregular wave conditions. FOC lagged behind, with higher THD levels that may jeopardize grid quality in rough sea states.

4.7.4. Discussion on Real-World Applicability

The deterministic analyses presented earlier characterize the inherent behavior of the STSMC strategy under ideal conditions. However, in realistic offshore deployments, two common types of disturbance can influence system performance: low-level sensor noise (SN) and slowly varying mooring dynamics (MD). SN is emulated by introducing small, zero-mean perturbations into the generator speed (ω_m) and current (i_q) feedback channels, simulating the drift and quantization effects typically encountered in marine instrumentation. MD is modeled as a linearized catenary response added to the heave equation, introducing a soft restoring force and damping that couple surge and heave motions.

Figure 14 presents a comparison of the generator speed response with and without SN. The sliding surface remains unaffected; only narrow-band, high-frequency oscillations appear around the reference signal, without introducing any sustained deviation. This demonstrates that the discontinuous structure of STSMC inherently suppresses small measurement disturbances without requiring additional compensation or retuning.

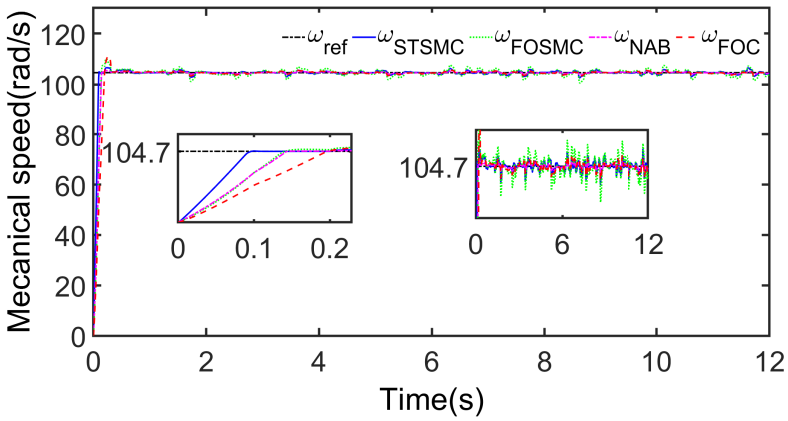


Figure 14. Generator speed ω_m with sensor noise using various control strategies under regular wave inputs. The shaded region illustrates the injected measurement jitter.

Figure 15 illustrates the electrical power P_e under the influence of MD. The slow oscillation of the mooring line induces gentle fluctuations near the nominal power level. Brief flat segments at the rated value (500 W) reflect the activation of the internal power-limiting function within the controller, designed to prevent overloading. These limit-induced plateaux are short in duration and do not push the system beyond safe operating limits. The overall power profile remains smooth, indicating that the controller tolerates mooring-induced variations without compromising performance.

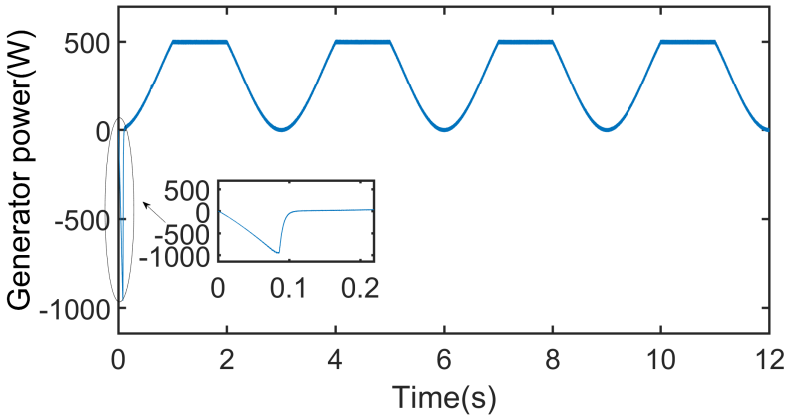


Figure 15. Electrical power P_e using STSMC under mooring dynamics. Short flat regions at the rated power level indicate activation of the internal power limiter.

These qualitative findings suggest that the proposed STSMC maintains its key advantages—fast dynamic response and stable power delivery—even in the presence of representative offshore disturbances. Future work will investigate broader disturbance scenarios, including cable dynamics in array configurations and time-varying delays in real-time embedded systems.

5. Conclusions

This paper presented a comprehensive model of a nonlinear heaving PAWEC with a PMSG and introduced an STSMC strategy to enhance both efficiency and stability. The overall wave-to-wire process was simulated in MATLAB/Simulink, encompassing wave energy capture and subsequent grid integration at 220 V, 50 Hz. Comparative results with conventional control methods—including FOC, NAB, and FOSMC—highlighted the notable advantages of STSMC.

The proposed STSMC demonstrated significant gains in response time, tracking precision, and robustness. Under regular wave conditions, it reached steady state up to 33% faster than FOC and reduced settling times by 20–50% relative to NAB and FOSMC. Under irregular wave conditions, STSMC sustained stable performance, mitigating steady-state errors and minimizing oscillations in torque, speed, and power output. Power quality analysis revealed that STSMC effectively controlled THD at approximately 3.49%, meeting typical grid standards.

These findings suggest that STSMC offers a promising control framework for practical wave energy applications, delivering higher reliability and efficiency for marine energy systems. Future efforts will focus on validating the proposed approach in real ocean environments to assess its adaptability, scalability, and long-term performance under authentic wave conditions.

Author Contributions: Conceptualization, Z.L. and L.W. (Lixian Wang); methodology, Z.L., L.W. (Lixian Wang), and L.W. (Lidong Wang); software, Z.L. and L.L.; validation, Z.L., L.W. (Lidong Wang), and X.L.; formal analysis, L.W. (Lixian Wang) and L.W. (Lidong Wang); investigation, Z.L.; resources, L.W. (Lidong Wang); data curation, Z.L. and Z.W.; writing—original draft preparation, Z.L.; writing—review and editing, X.L. and L.W. (Lidong Wang); supervision, L.W. (Lidong Wang) and X.L.; project administration, L.W. (Lidong Wang) and X.L.; visualization, Z.L. All authors have read and agreed to the published version of the manuscript.

Funding: This work was supported by the Fundamental Research Funds for Liaoning Provincial Joint Funds Project–General Funding Program (Grant Nos. 2023-MSLH-323 and 2023-MSLH-310); the Fundamental Research Funds for Liaoning Universities (LJ212410146009); the Foundation of Yingkou Automation Industrial Control Professional Technology Innovation Center (Grant No. AICPTI01); the Foundation of Yingkou Institute of Technology under the Institutional-Level Scientific Research Initiative (Grant Nos. FDL202404 and FDL202409); the National Natural Science Foundation of China (Grant Nos. 62173127 and 62472143); the Key Research and Development Special Projects in Henan Province (Grant No. 241111521000); and the Top Young Talents Program in Central Plains (Grant No. (2023)11).

Institutional Review Board Statement: Not applicable.

Informed Consent Statement: Not applicable.

Data Availability Statement: The data presented in this study are available on request from the corresponding author. The data are not publicly available due to privacy or ethical restrictions.

Conflicts of Interest: The authors declare no conflicts of interest.

Nomenclature

The following nomenclatures are used in this paper.

Nomenclature	Definition
PAWEC	Point absorber wave energy converter
PMSG	Permanent magnet synchronous generator
PTO	Power take-off
FOC	Field-oriented control
FOSMC	First-order sliding-mode control
STSMC	Super-twisting sliding-mode control
NAB	Nonlinear adaptive backstepping
MPPT	Maximum power point tracking
THD	Total harmonic distortion
MMR	Mechanical motion rectification
PLL	Phase-locked loop
SVPWM	Space vector pulse-width modulation
PM	Pierson–Moskowitz spectrum
JONSWAP	Joint North Sea Wave Project spectrum
H	Wave height [m]
ω	Angular frequency of ocean wave [rad s^{-1}]
k	Wave number [rad m^{-1}]
$z(t)$	Buoy heave displacement [m]
$F_e(t)$	Wave excitation force [N]
m_b	Buoy dry mass [kg]
m_a	Added mass [kg]
ρ	Water density [kg m^{-3}]
g	Gravitational acceleration [m s^{-2}]
A	Waterplane area [m^2]
k_{PTO}	PTO stiffness coefficient [N m^{-1}]
c_{PTO}	PTO damping coefficient [N s m^{-1}]
T_m	Mechanical torque [N m]
T_e	Electromagnetic torque [N m]
J	System inertia [kg m^2]
f_d	Damping coefficient [N m s rad^{-1}]
p	Number of pole pairs
ψ_f	Flux linkage [Wb]
R_s	Stator resistance [Ω]
L_d, L_q	d-axis, q-axis inductances [H]
i_d, i_q	d-axis, q-axis stator currents [A]
v_d, v_q	d-axis, q-axis stator voltages [V]
ω_e	Electrical angular velocity [rad s^{-1}]
V_{dc}	DC link voltage [V]
η_{inverter}	Inverter efficiency
P_{elec}	Electrical power output [W]
P_{AC}	AC power [W]
P_{grid}	Power delivered to grid [W]
V_{grid}	Grid voltage [V]
I_{grid}	Grid current [A]
θ	Phase angle between voltage and current [rad]

References

1. Darwish, A.; Aggidis, G.A. A Review on Power Electronic Topologies and Control for Wave Energy Converters. *Energies* **2022**, *15*, 9174. [CrossRef]
2. Guo, B.; Ringwood, J.V. A review of wave energy technology from a research and commercial perspective. *IET Renew. Power Gener.* **2021**, *15*, 3065–3090. [CrossRef]
3. Guo, B.; Wang, T.; Jin, S.; Duan, S.; Yang, K.; Zhao, Y. A review of point absorber wave energy converters. *J. Mar. Sci. Eng.* **2022**, *10*, 1534. [CrossRef]

4. Ozkop, E.; Altas, I.H. Control, power and electrical components in wave energy conversion systems: A review of the technologies. *Renew. Sustain. Energy Rev.* **2017**, *67*, 106–115. [CrossRef]
5. He, G.; Luan, Z.; Zhang, W.; He, R.; Liu, C.; Yang, K.; Yang, C.; Jing, P.; Zhang, Z. Review on research approaches for multi-point absorber wave energy converters. *Renew. Energy* **2023**, *218*, 119237. [CrossRef]
6. Prasad, K.A.; Chand, A.A.; Kumar, N.M.; Narayan, S.; Mamun, K.A. A critical review of power take-off wave energy technology leading to the conceptual design of a novel wave-plus-photon energy harvester for island/coastal communities' energy needs. *Sustainability* **2022**, *14*, 2354. [CrossRef]
7. Zhang, Y.; Zhao, Y.; Sun, W.; Li, J. Ocean wave energy converters: Technical principle, device realization, and performance evaluation. *Renew. Sustain. Energy Rev.* **2021**, *141*, 110764. [CrossRef]
8. Wang, L.; Isberg, J.; Tedeschi, E. Review of control strategies for wave energy conversion systems and their validation: The wave-to-wire approach. *Renew. Sustain. Energy Rev.* **2018**, *81*, 366–379. [CrossRef]
9. Tan, J.; Polinder, H.; Laguna, A.J.; Miedema, S. A wave-to-wire analysis of the adjustable draft point absorber wave energy converter coupled with a linear permanent-magnet generator. *Ocean. Eng.* **2023**, *276*, 114195. [CrossRef]
10. Kristiansen, E.; Hjulstad, Å.; Egeland, O. State-space representation of radiation forces in time-domain vessel models. *Ocean. Eng.* **2005**, *32*, 2195–2216. [CrossRef]
11. Tan, J.; Tao, W.; Laguna, A.J.; Polinder, H.; Xing, Y.; Miedema, S. A spectral-domain wave-to-wire model of wave energy converters. *Appl. Ocean. Res.* **2023**, *138*, 103650. [CrossRef]
12. Penalba, M.; Ringwood, J.V. A high-fidelity wave-to-wire model for wave energy converters. *Renew. Energy* **2019**, *134*, 367–378. [CrossRef]
13. Lin, Z.; Zhou, J.; Huang, X.; Chen, K.; Xiao, X.; Ringwood, J.V. On Loss-Aware Optimal Control of Wave Energy Converters With Electrical Power Take-Offs. *IEEE Trans. Sustain. Energy* **2024**, *15*, 2209–2218. Available online: https://ieeexplore.ieee.org/abstract/document/10542448 (accessed on 21 June 2025). [CrossRef]
14. Haider, A.S.; Brekken, T.K.; Coe, R.G.; Bacelli, G.; McCall, A. On real-time hybrid testing of ocean wave energy conversion systems: An experimental study. *IEEE Open J. Ind. Appl.* **2022**, *3*, 30–40. Available online: https://ieeexplore.ieee.org/abstract/document/9705552 (accessed on 21 June 2025). [CrossRef]
15. El Mourabit, Y.; Derouich, A.; El Ghzizal, A.; El Ouanjli, N.; Zamzoum, O. Nonlinear backstepping control for PMSG wind turbine used on the real wind profile of the Dakhla-Morocco city. *Int. Trans. Electr. Energy Syst.* **2020**, *30*, e12297. [CrossRef]
16. Yin, X.; Li, X.; Zuo, L. Dynamic characteristics and test results of a wave power takeoff system with mechanical motion rectification and transmission. *IEEE Trans. Ind. Electron.* **2019**, *68*, 12262–12271. Available online: https://ieeexplore.ieee.org/abstract/document/8633865 (accessed on 21 June 2025). [CrossRef]
17. Noman, M.; Li, G.; Wang, K.; Han, B. Electrical control strategy for an ocean energy conversion system. *Prot. Control Mod. Power Syst.* **2021**, *6*, 1–18. Available online: https://ieeexplore.ieee.org/abstract/document/10372543 (accessed on 21 June 2025). [CrossRef]
18. Demonte Gonzalez, T.; Parker, G.G.; Anderlini, E.; Weaver, W.W. Sliding mode control of a nonlinear wave energy converter model. *J. Mar. Sci. Eng.* **2021**, *9*, 951. [CrossRef]
19. M'zoughi, F.; Garrido, I.; Garrido, A.J.; De la Sen, M. Fuzzy gain scheduled-sliding mode rotational speed control of an oscillating water column. *IEEE Access* **2020**, *8*, 45853–45873. [CrossRef]
20. Zhang, Y.; Li, G. Non-causal linear optimal control of wave energy converters with enhanced robustness by sliding mode control. *IEEE Trans. Sustain. Energy* **2019**, *11*, 2201–2209. Available online: https://ieeexplore.ieee.org/abstract/document/8894532 (accessed on 21 June 2025). [CrossRef]
21. Barambones, O.; Cortajarena, J.A.; de Durana, J.M.G.; Alkorta, P. A real time sliding mode control for a wave energy converter based on a wells turbine. *Ocean Eng.* **2018**, *163*, 275–287. [CrossRef]
22. Magaña, M.E.; Danielle, R. Sliding mode control of an array of three oscillating water column wave energy converters to optimize electrical power. In Proceedings of the European Wave and Tidal Energy Conference, Napoli, Italy, 1–6 September 2019.
23. Gaebele, D.T.; Magana, M.E.; Brekken, T.K.; Henriques, J.C.; Carrelhas, A.A.; Gato, L.M. Second order sliding mode control of oscillating water column wave energy converters for power improvement. *IEEE Trans. Sustain. Energy* **2020**, *12*, 1151–1160. Available online: https://ieeexplore.ieee.org/abstract/document/9247304 (accessed on 21 June 2025). [CrossRef]
24. Zhang, Y.; Zeng, T.; Li, G. Robust excitation force estimation and prediction for wave energy converter M4 based on adaptive sliding-mode observer. *IEEE TRansactions Ind. Inform.* **2019**, *16*, 1163–1171. [CrossRef]
25. Zou, S.; Song, J.; Abdelkhalik, O. A sliding mode control for wave energy converters in presence of unknown noise and nonlinearities. *Renew. Energy* **2023**, *202*, 432–441. [CrossRef]
26. Moghaddam, R.K.; Mohamadie, N.K. Fast terminal nonsingular sliding mode control of wave energy converters for maximum power absorption. *Ocean. Eng.* **2023**, *281*, 114473. [CrossRef]
27. Mosquera, F.; Faedo, N.; Evangelista, C.; Puleston, P.; Ringwood, J. Energy-maximising tracking control for a nonlinear heaving point absorber system commanded by second order sliding modes. *IFAC-PapersOnLine* **2022**, *55*, 357–362. [CrossRef]

28. Mosquera, F.D.; Evangelista, C.A.; Puleston, P.F.; Ringwood, J.V. Adaptive second order sliding mode control of an oscillating water column. *IET Renew. Power Gener.* **2024**, *18*, 226–237. [CrossRef]
29. Amine, H.M.; Othmane, A.; Saad, M. The impacts of control systems on hybrid energy storage systems in remote DC-Microgrid system: A comparative study between PI and super twisting sliding mode controllers. *J. Energy Storage* **2022**, *47*, 103586. [CrossRef]
30. Faedo, N.; Mosquera, F.D.; Pasta, E.; Papini, G.; Peña-Sanchez, Y.; Evangelista, C.A.; Ferri, F.; Ringwood, J.V.; Puleston, P. Experimental assessment of combined sliding mode & moment-based control (SM2C) for arrays of wave energy conversion systems. *Control Eng. Pract.* **2024**, *144*, 105818. [CrossRef]
31. Al-Dhaifallah, M.; Ahmed, A.M.; Hasanien, H.M.; Ali, Z.M.; Ebrahim, E.A.; Aleem, S.H.A. Dynamic performance enhancement of nonlinear AWS wave energy systems based on optimal super-twisting control strategy. *Ain Shams Eng. J.* **2024**, *15*, 102732. [CrossRef]
32. Mosquera, F.; Faedo, N.; Evangelista, C.; Ringwood, J.; Puleston, P. Wave Energy Optimal Control Structure With Second-Order Sliding Mode Tracking: Hardware-in-the-Loop Assessment. *IEEE Trans. Sustain. Energy* **2023**, *15*, 1341–1350. Available online: https://ieeexplore.ieee.org/abstract/document/10363673 (accessed on 21 June 2025). [CrossRef]
33. Wang, Z.; Luan, F.; Wang, N. An improved model predictive control method for wave energy converter with sliding mode control. *Ocean. Eng.* **2021**, *240*, 109881. [CrossRef]
34. Davidson, J.; Genest, R.; Ringwood, J.V. Adaptive control of a wave energy converter. *IEEE Trans. Sustain. Energy* **2018**, *9*, 1588–1595. [CrossRef]
35. Jia, Y.; Sun, J.; Xu, Z.; Sun, C.; Meng, K.; Dong, Z.Y. Data-driven economic MPC of a point absorber wave energy converter. *IEEE J. Emerg. Sel. Top. Ind. Electron.* **2024**, *5*, 670–679. [CrossRef]
36. Manikandan, R.; Chaudhuri, P.; Sakthivel, R. Numerical modelling and backstepping-based control of barge platform-supported offshore wind turbines under wind and wave loads. *Ships Offshore Struct.* **2025**, 1–14. [CrossRef]
37. Berkani, A.; Ghazwani, M.H.; Negadi, K.; Hadji, L.; Alnujaie, A.; Ghazwani, H.A. Predictive control and modeling of a point absorber wave energy harvesting connected to the grid using a LPMSG-based power converter. *Ocean. Syst. Eng.* **2024**, *14*, 17–52. [CrossRef]
38. Weng, S.; Wang, J. A Novel Back-Stepping Sliding Mode Control Strategy of Direct-Drive Wave Energy Converters. *Processes* **2022**, *10*, 1385. [CrossRef]
39. Zhao, K.; Jia, N.; She, J.; Dai, W.; Zhou, R.; Liu, W.; Li, X. Robust model-free super-twisting sliding-mode control method based on extended sliding-mode disturbance observer for PMSM drive system. *Control Eng. Pract.* **2023**, *139*, 105657. [CrossRef]
40. Karafyllis, I.; Jiang, Z.P. *Stability and Stabilization of Nonlinear Systems*; Springer Science & Business Media: Berlin/Heidelberg, Germany, 2011. [CrossRef]
41. Suchithra, R.; Ezhilsabareesh, K.; Samad, A. Optimization based higher order sliding mode controller for efficiency improvement of a wave energy converter. *Energy* **2019**, *187*, 116111. [CrossRef]
42. Filippov, A.F. *Differential Equations with Discontinuous Righthand Sides: Control Systems*; Springer Science & Business Media: Berlin/Heidelberg, Germany, 2013; Volume 18. [CrossRef]

Disclaimer/Publisher's Note: The statements, opinions and data contained in all publications are solely those of the individual author(s) and contributor(s) and not of MDPI and/or the editor(s). MDPI and/or the editor(s) disclaim responsibility for any injury to people or property resulting from any ideas, methods, instructions or products referred to in the content.